

Deciphering Ni sequestration in soil ferromanganese nodules by combining X-ray fluorescence, absorption, and diffraction at micrometer scales of resolution

ALAIN MANCEAU,^{1,2,*} NOBUMICHI TAMURA,¹ MATTHEW A. MARCUS,¹ ALASTAIR A. MACDOWELL,¹ RICHARD S. CELESTRE,¹ ROBERT E. SUBLETT,¹ GARRISON SPOSITO,³ AND HOWARD A. PADMORE¹

¹Advanced Light Source, Lawrence Berkeley National Laboratory, One Cyclotron Road, Berkeley, California 94720, U.S.A.

²Environmental Geochemistry Group, LGIT, University J. Fourier and CNRS, 38041 Grenoble Cedex 9, France

³Geochemistry Department, Earth Sciences Division, Lawrence Berkeley National Laboratory, University of California, Berkeley, California 94720, U.S.A.

ABSTRACT

X-ray microprobes are among the most important new analytical techniques to emerge from third generation synchrotron facilities. Here we show how X-ray fluorescence, diffraction, and absorption can be used in parallel to determine the structural form of trace elements in heterogeneous matrices at the micrometer-scale of resolution. Scanning X-ray microfluorescence (μ SXRF) and microdiffraction (μ SXRD) first are used to identify the host solid phase by mapping the distributions of elements and solid species, respectively. Micro-extended X-ray absorption fine structure (μ EXAFS) spectroscopy is then used to determine the mechanism of trace element binding by the host phase at the molecular scale. To illustrate the complementary application of these three techniques, we studied how nickel is sequestered in soil ferromanganese nodules, an overwhelmingly complex natural matrix consisting of submicrometer to nanometer sized particles with varying structures and chemical compositions. We show that nickel substitutes for Mn^{3+} in the manganese layer of the MnO_2 - $Al(OH)_3$ mixed-layer oxide lithiophorite. The affinity of Ni for lithiophorite was characteristic of micronodules sampled from soils across the U.S.A. and Europe. Since many natural and synthetic materials are heterogeneous at nanometer to micrometer scales, the synergistic use of μ SXRF, μ SXRD, and μ EXAFS is expected to have broad applications to earth and materials science.

INTRODUCTION

Environmental materials are intrinsically complex, being chemically and structurally heterogeneous at all scales, and their study poses a challenge for investigating metal speciation using conventional techniques. The main difficulties are the partitioning of trace elements into coexisting mineral phases, the identification of the mineral species to which these elements are bound, and the multiplicity of uptake mechanisms. In the absence of robust analytical techniques that could reliably identify and quantify each chemical species, operationally defined chemical extractions have been developed during the last two decades, and several procedures have been certified for quality assurance by the Commission of the European Communities Bureau of Reference (Quevauviller et al. 1994). In these methods, chemical reagents of various strengths are used to break the binding forces and to liberate and subsequently extract the metals from the mineral phases. However, uncertainties remain related to the selectivity of the various extractants and to potential problems due to re-adsorption of the dissolved metal by other phases (Gomez-Ariza et al. 2000; Ho and Evans 2001; Ostergren et al. 1999). Several physical techniques are also used to investigate the crystal chemistry of trace metal impurities in solids, of which electron microscopy (Buseck 1992) and bulk extended X-ray absorption fine structure (EXAFS) (Brown et al. 1999; Manceau et al. 2002) are among the most efficient.

However, as powerful and, as often used as these methods are, none of them separately or together allow one to identify both the nature of the host species and the incorporation mechanism of trace metals at the molecular scale. In the most advanced application of EXAFS spectroscopy to speciation, the number and nature of metal species are rigorously evaluated by principal component analysis (PCA) of a set of experimental spectra. Their proportions subsequently are estimated by least-squares fitting (LSF) of experimental data to the combination of reference spectra previously identified by PCA. Still, PCA is a wholly statistical analytical treatment of a set of mixed spectra, and the quantification procedure requires that all individual species are present in the reference database. As with any desummation technique, there can also be some concerns about the uniqueness of the analysis. In addition, there is no direct link to the actual solid phases (mineral or organic) present in the sample. X-ray micro-diffraction and micro-fluorescence, as an adjunct to EXAFS spectroscopy, ground this multicomponent spectral analysis in reality, obviating the need for any guesswork. Synchrotron-based scanning X-ray microfluorescence (μ SXRF) (Sutton and Rivers 1999) and microdiffraction (μ SXRD) (Tamura et al. 2002) together allow one to visualize the two-dimensional distribution of metals in minerals, and hence to determine to which particular mineral a given metal is bound, by simultaneous imaging of elemental and mineral distributions within the heterogeneous matrix. The coordination chemistry of the metal, and hence its incorporation mechanism within the mineral host, then is identified by μ EXAFS

* E-mail: Alain.Manceau@ujf-grenoble.fr

performed on single metal species.

The power of combined fluorescence-diffraction-absorption studies at micrometer-scale resolution is illustrated here by determining how Ni is sequestered in soil ferromanganese nodules. Soils represent a major sink for anthropogenic Ni, and its migration to living organisms is an environmental concern because of its suspected carcinogenicity when it is speciated as nickel sulfate or combinations of nickel sulfides and oxides, provoking lung and nasal cancers (Nriagu 1980; Yaman 2000). The anthropogenic nickel sources are metal processing operations, combustion of coal and oil, and sewage sludge. The crystal chemistry of nickel in oxidized and silicated ores has been abundantly studied for economic reasons, and in these formations Ni is predominantly associated with phyllosilicates and the Fe oxyhydroxide goethite (α -FeOOH). During its journey from the source to its resting place in soils, Ni can undergo many chemical transformations, and understanding how this element is naturally sequestered helps provide a solid scientific basis for maintaining soil quality and formulating educated strategies to remediate severely impacted areas. The most efficient and durable process responsible for trace metal sequestration in soils is the formation of ferromanganese micronodules, which have often been compared to the well-known oceanic Mn nodules (Glasby et al. 1979; Han et al. 2001; White and Dixon 1996). Although soil micronodules are the premier reservoir for trace metals in soils, the crystal chemistry of the sequestered elements remains poorly understood (Manceau et al. 2002). Nickel is of special interest because chemical analyses of individual nodules from Sicilia and New Zealand showed that this element is enriched in these concretions relative to the soil matrix (Childs 1975; Palumbo et al. 2001). The micronodules studied here were collected in the plowed layer of agricultural fields of the Morvan region (France) used for livestock breeding activities (Baize and Chrétien 1994; Latrille

et al. 2001). Soils in this area are developed on the Sinemurian calcareous geological setting, and contain 5–12 weight percent of ferromanganese pellets termed “shot”, “lead shot”, or “buck-shot” by agriculturists (Baize and Chrétien 1994; Wheating 1936). The nodules are enriched in most trace metals [Ni = 534 (σ = 99), Zn = 4063 (σ = 1393), Pb = 1423 (σ = 1234) mg/Kg; Latrille et al. 2001], but fixed in a form which makes them highly immobile and thus not very accessible to living organisms (i.e., not harmful).

EXPERIMENTAL METHODS

X-ray diffraction patterns and fluorescence spectra were recorded at fixed energy at Beamline 7.3.3 at the Advanced Light Source (ALS, Berkeley), and then fluorescence X-ray absorption spectra were collected at Beamline 10.3.2 by varying the energy of the incident beam (MacDowell et al. 2001; Padmore et al. 1996) (Fig. 1). At both beamlines, the source is first imaged at 1:1 magnification with a toroidal mirror to a maximum spot size of $240 \times 35 \mu\text{m}$, determined by the source size. This “virtual source” is then imaged by two elliptically bent mirrors, arranged in the Kirkpatrick-Baez (KB) crossed configuration (Kirkpatrick and Baez 1948). The demagnification of this mirror pair is 28.3 horizontal (H) \times 12.5 vertical (V) (7.3.3) and 20 (H) \times 6 (V) (10.3.2). The spot size on the sample is adjusted with slits placed at the virtual source so as to trade flux for lateral resolution. The divergence of the beam after the KB mirrors is $3.7 \times 1.6 \text{ mrad}$ (7.3.3) or $4.1 \times 1.7 \text{ mrad}$ (10.3.2). For micro-spectroscopy (10.3.2), an additional parabolic mirror collimates the incoming beam in the vertical direction to match the vertical divergence of the beam to the monochromator. It is very important, especially when doing μEXAFS , to keep the beam position stable as a function of energy. If the beam drifts on or off micrometer-sized features in the samples, the resulting signal variation could mimic

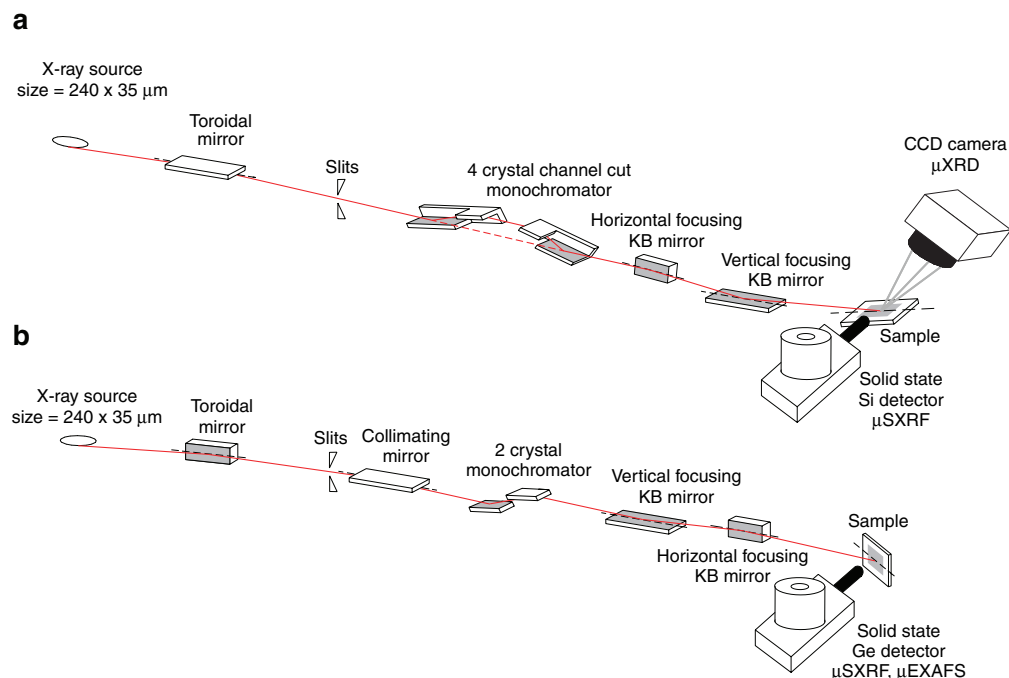


FIGURE 1. Schematic diagram of the experimental setups used on stations 7.3.3. (a) and 10.3.2 (b) of the ALS for combined X-ray fluorescence and diffraction (a), and X-ray fluorescence and absorption (b) measurements (MacDowell et al. 2001; Padmore et al. 1996).

EXAFS features, thus invalidating the analysis. The monochromators in the two beamlines are both designed to keep the beam position and angle stable, but in different ways. The 7.3.3 monochromator consists of two channel-cut Si(111) crystals mounted in a dispersive arrangement such that the energy is varied by rotating the crystal pairs in opposite directions. The second pair is slaved to the first via a tape-drive mechanism, which has proven to be highly stable. "Tweaking" of the relative orientations of the pairs has proven to be unnecessary. The 10.3.2 monochromator consists of two Si(111) crystals mounted on a common rotation stage. To maintain a fixed exit position, the second crystal is moved relative to the first in a direction perpendicular to its diffracting surface. This motion is accomplished by a flexure linkage, which keeps the crystals parallel over a wide energy range with no adjustment.

The distribution of nanometer-sized particles, which are the most reactive toward metal sorption, was imaged at a resolution of $20 \times 20 \mu\text{m}$ by collecting point powder XRD patterns and integrating the diffracted intensity along the Debye rings. XRD patterns were conveniently measured alongside fluorescence spectra using a large-area CCD camera (Bruker 6000, active area of $9 \times 9 \text{ cm}$) placed above the specimen stage (Fig. 1a). Samples were prepared as $30 \mu\text{m}$ thick micropolished thin sections adhered to glass slides and inclined at 6° to the horizontal plane. At this angle, the lateral size of the illuminated area was $14 \mu\text{m}$ (H) \times $11 \mu\text{m}$ (V). In principle, diffraction data

may be collected in transmission mode with photon energies of about 10–12 keV, but in practice the best results were obtained by recording the data in reflection mode with an excitation energy (6.3 keV) below the absorption edge of transition metals present in the matrix (Mn, Fe, Ni, Zn). This is because at higher energy the fluorescence signal from Mn and Fe enters the detector, thereby adding to the background noise of the diffraction patterns. The distance between the analyzed spot on the sample and the CCD, and the 2θ scale were precisely calibrated using the reflection peaks of quartz grains contained in the sample. Fluorescence maps were obtained by scanning the sample stage under the monochromatic beam at $E = 10 \text{ keV}$ with a step size of $20 \times 20 \mu\text{m}$, while recording the X-ray fluorescence with a Si (7.3.3) or Ge (10.3.2) solid-state detector. Fluorescence-yield nickel *K*-edge μEXAFS spectra were then collected from single metal species aggregates at $16 \mu\text{m H} \times 5 \mu\text{m V}$ resolution. Measurements were carried out by orienting the sample vertically to 45° to both the X-ray beam and the solid-state detector (Fig. 1b). μSXRF maps were also recorded in this geometry to re-image the areas previously identified by μSXRD - μSXRF .

RESULTS AND DISCUSSION

Figure 2 shows how laterally resolved μSXRF and μSXRD data can be used to identify the partitioning of trace elements among coexisting mineral phases within their natural matrix.

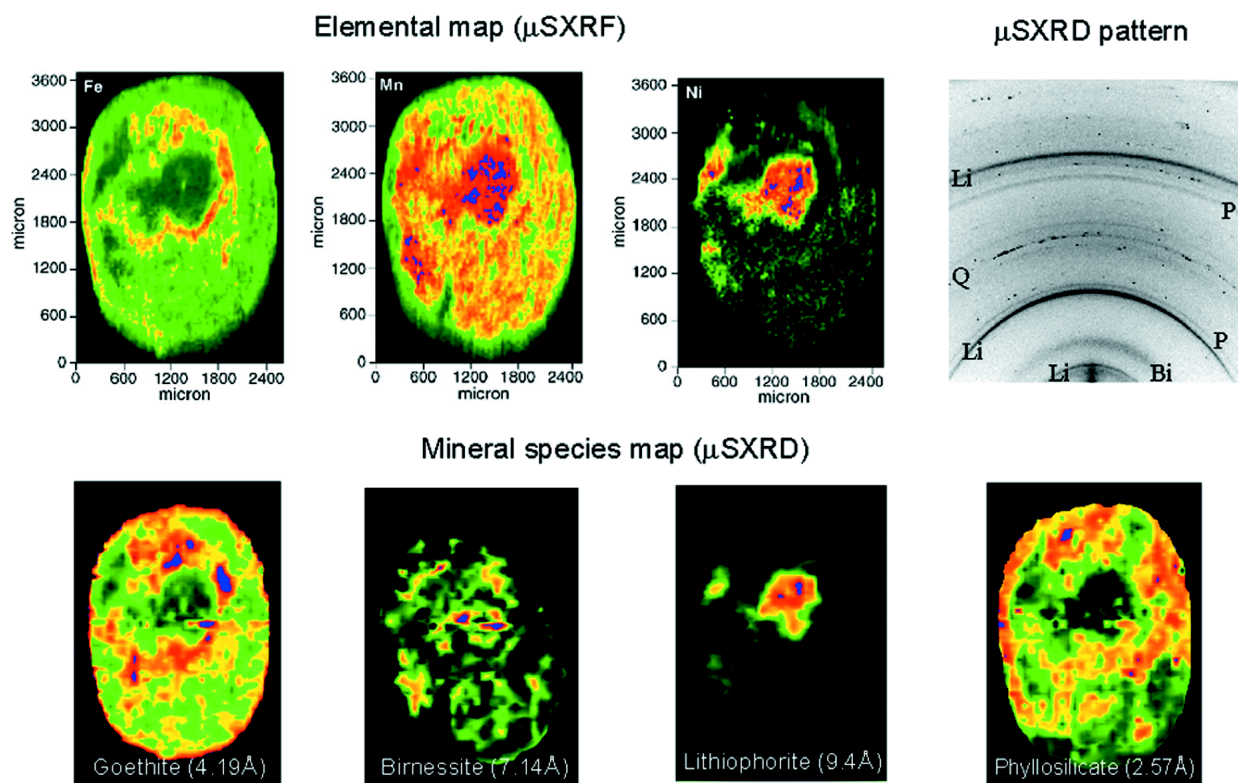


FIGURE 2. Combined fluorescence-diffraction measurements recorded on a ferromanganese soil nodule (sample TN4 from Baize and Chrétien 1994 and Latrille et al. 2001). The three images on the top are elemental maps obtained by μSXRF , and the four images on the bottom are mineral species maps obtained by integrating at each point of analysis the intensities of the relevant (*hkl*) reflections along the Debye rings of the two-dimensional XRD patterns (*d*-spacings are indicated in parenthesis). One XRD pattern is presented top right. Li = lithiophorite, Bi = birnessite, P = phyllosilicate, Q = quartz.

With μ SXRF the distribution of Fe, Mn, and Ni were determined, and it was found that Mn and Ni were systematically associated in the six different soil nodules examined in this study. Two-dimensional XRD patterns were characterized by the presence of point diffraction spots from sub-micrometer crystals, including quartz, feldspar, titanium oxide, illite, and kaolinite, and continuous Debye rings arising from nanometer-sized particles, including phyllosilicate, goethite (α -FeOOH), and three Mn oxides, lithiophorite, birnessite, and Fe-vernadite (Fig. 2). The mineral abundance maps of the first four finely divided (nanometer-sized) species were produced by integrating at each point-of-analysis the diffracted intensities of the non-overlapping (020) and (200) reflections at ~ 4.45 and ~ 2.57 Å for phyllosilicates, the (101) and (301) reflections at 4.19 Å and 2.69 Å for goethite, the (001) reflection at 7.1–7.2 Å for birnessite, and the (001) and (002) reflections at 9.39 Å and 4.69 Å for lithiophorite. Kaolinite and illite grains generate intense reflection maxima at 7.14 Å, and ~ 4.46 Å and ~ 2.57 Å, respectively, which overlap with reflections from birnessite and nanometer-sized phyllosilicate particles (smectitic clays). This difficulty in the mineralogical analysis of soils is well-known and has often prevented the unambiguous identification of these minerals by conventional XRD analysis (Rhoton et al. 1993; Taylor et al. 1964; Tokashiki et al. 1986). Since kaolinite and illite grains are comparable in size to the X-ray beam, they yield strongly textured two-dimensional μ XRD patterns, which contrast with the powder XRD patterns from minute particles, allowing one to separate analytically the two types of patterns in two-dimensional μ XRD experiments. The reliability of this quantitative treatment was verified by comparing mineral maps calculated using independent (*hkl*) reflections of the same mineral species. The distribution of Fe-vernadite, a common soil mineral (Chukhrov and Gorshkov 1981; Vodyanitskii et al. 2001), was not mapped because it was systematically detected throughout the examined nodules without any significant concentration gradient. This Fe-Mn disordered phase (also termed Mn-feroxyhite), which is dispersed throughout the nodule matrix filling pores and aggregating coarse grains, acts as a cementing agent for the nodules. Comparison of the μ SXRF and μ SXRD maps shows that nickel and lithiophorite have the same distribution, therefore suggesting that Ni is bound to this particular mineral phase. However, it should be noted that an association between an element *E* and a mineral *M* does not necessarily imply that *E* is chemically bound to or included in the structure of *M*. Still, we shall see from the EXAFS results that Ni is indeed included in the lithiophorite structure. We note that this nodule contains regions in which birnessite and lithiophorite coexist, therefore the recording of point- μ XRD patterns in these regions would not be conclusive regarding the partitioning of nickel between these two minerals. This finding demonstrates the usefulness of combining element and mineral maps, and shows that pertinent information can be obtained from nanometer-sized environmental particles at the micrometer-scale of resolution because of their segregation in localized areas. In this case, the heterogeneity of environmental samples becomes an advantage. That goethite is devoid of nickel is also clearly apparent from these maps, which show that the goethite “crown” area contains no nickel.

The systematic association of Ni with lithiophorite suggests that Ni should be located in a definite cation site of the manganese oxide crystal structure. Lithiophorite has a layered structure consisting of alternating MnO_2 and $\text{Al}(\text{OH})_3$ octahedral layers, in which, ideally, all Mn sites are occupied and one third of Al sites are empty or occupied by Li (dioctahedral structure, Fig. 3). Phyllosilicates, however, are rarely stoichiometric, and can accommodate big aliovalent cations (Li^+ , Ni^{2+} , Cu^{2+} , Zn^{2+}) in the vacant Al sites, and Mn^{3+} ions in the Mn^{4+} sites. For electrostatic reasons, the resulting positive net charge of the $\text{Al}(\text{OH})_3$ layer and the negative net charge of the MnO_2 layer contribute to increase the stability of the mixed-layer framework by increasing the strength of hydrogen bonds. To determine the exact Ni site, Ni *K*-edge μ EXAFS spectra were collected from Ni-rich regions from several nodules. All spectra were identical, indicating that the incorporation mechanism of Ni is unique, and is the key to understanding its sequestration in soils. Qualitative information about the local structure of Ni can be obtained by comparing the unknown μ EXAFS spectrum to reference EXAFS spectra from relevant model compounds. As expected from μ SXRF- μ SXRD experiments, the two reference spectra for Ni in goethite (Manceau et al. 2000) and phyllosilicates (Manceau and Calas 1986) did not match the unknown spectrum, confirming that Ni is not sequestered in these forms (data not shown). Differences in frequency and shape of the EXAFS oscillations were also observed with birnessite, in which Ni is sorbed above vacant Mn sites,

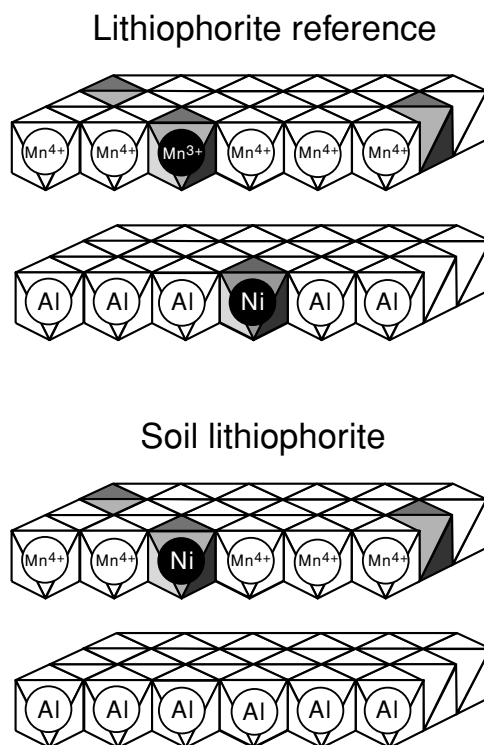


FIGURE 3. Structure of lithiophorite and incorporation mechanism of nickel in the reference and soil lithiophorite specimen.

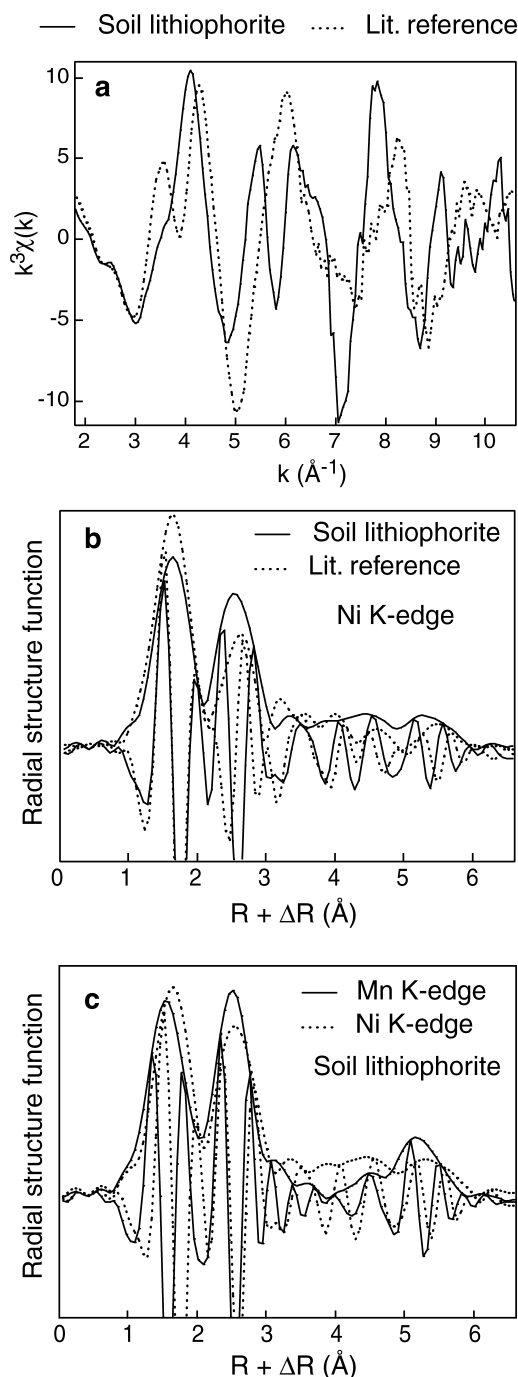


FIGURE 4. Ni K-edge μ EXAFS spectrum (a) and Fourier transform (modulus plus imaginary part) (b, c) from a "hot spot" of the core of the nodule, compared to the Ni- and Mn-edge data from a Ni-containing lithiophorite reference, in which Ni substitutes for Li in the $\text{Al}(\text{OH})_3$ layer (Manceau et al. 1987). The peaks in the Fourier transforms are not at their exact expected positions (R values) because of phase-shift effects (ΔR) and disorder arising from the accommodation of atoms having different radii. The Ni-Mn and Mn-Mn contributions at $R + \Delta R = 2.5 \text{ \AA}$ in c) are almost superimposed (both the modulus and imaginary parts), indicating that the cationic environment of Ni is akin to that of Mn. This is strong evidence that Ni is present at the Mn site in the lithiophorite structure.

and with lithiophorite, in which Ni is located within the gibbsitic Al layer (Manceau et al. 1987) (Fig. 4a). Figure 4a shows that despite the arguments given above for assigning the Ni sorption site to lithiophorite, the EXAFS pattern observed in the soil does not agree with that from the reference sample of Ni in lithiophorite. However, that reference represents one possible mode of incorporation for Ni in this mineral, in which the Ni is in the gibbsitic $\text{Al}(\text{OH})_3$ layer. We shall now show that we can account for the observed spectrum by assuming another position for Ni in lithiophorite.

The radial structure functions (RSFs) obtained by Fourier transforming EXAFS spectra for the reference and the soil lithiophorite both exhibit, after the first oxygen peak, a second peak at roughly $R + \Delta R = 2.6 \text{ \AA}$, that is at a distance characteristic of edge-sharing linkage between metal octahedra (Fig. 4b). This result alone suggests that Ni is located within one of the two octahedral layers of the lithiophorite structure. To solve this issue, it is necessary to examine the phase of the imaginary part of the Fourier transform, because waves backscattered by Al and Mn atoms are almost out of phase (Teo 1986). Examination of Figure 4b shows that the unknown and lithiophorite reference have their electronic waves shifted by $\sim \pi$ in the $2.2\text{--}3.1 \text{ \AA}$ $R + \Delta R$ interval, thus indicating that Ni is substituted for Mn in the soil lithiophorite. In keeping with this conclusion, the two waves are logically in phase in the $1.0\text{--}2.2 \text{ \AA}$ $R + \Delta R$ interval, since in both structures Ni is octahedrally coordinated to oxygen atoms. Crystallographic distances obtained by least-squares fitting of the experimental data with the WINXAS program (Ressler 1998) and using amplitude and phase shift functions calculated with FEFF (Rehr et al. 1991), were $d(\text{Ni-O}) = 2.05 \text{ \AA}$, $d(\text{Ni-Mn}) = 2.91 \text{ \AA}$, $d(\text{Mn-O}) = 1.92 \text{ \AA}$, and $d(\text{Mn-Mn}) = 2.92 \text{ \AA}$. There was no indication of Ni-Ni pairs, for which Ni-Ni distances of 3.03 \AA to 3.12 \AA would be predicted (Manceau et al. 2000). This result indicates that nickel did not precipitate as a hydroxide, hence confirming that the next-nearest coordination shell of Ni is composed of Mn atoms.

Since Ni^{2+} has an effective radius 30% greater than that of Mn^{4+} (Shannon 1976), one may wonder how the Ni-Mn substitution is realized. To answer this question, Ni- and Mn-RSFs were plotted together (Fig. 4c), and the Ni- and Mn-EXAFS interatomic distances compared. A distinct feature in the Ni-RSF is the shift to higher $R + \Delta R$ values of the Ni-O peak, indicative of a relaxation of the Ni site owing to the larger size of the Ni^{2+} impurity ($r = 0.69 \text{ \AA}$) relative to Mn^{4+} ($r = 0.53 \text{ \AA}$) and Mn^{3+} ($r = 0.645 \text{ \AA}$). Since Ni^{2+} and Mn^{3+} have a size mismatch of only 7%, nickel likely substitutes at the trivalent manganese site. Likewise, the Al^{3+} site of the gibbsitic layer is clearly too small ($r = 0.535 \text{ \AA}$) to accommodate Ni^{2+} , and the larger Li^+ site ($r = 0.76 \text{ \AA}$) is probably energetically less favorable. This assumption is supported by recent atomistic calculations and EXAFS measurements on lanthanide-doped perovskite, which showed that the rare earth element is energetically stabilized in smaller crystallographic sites (Davies et al., 2000). The same results were obtained on nodules from flood plain soils in the U.S.A., which suggests that the Ni species identified herein may correspond to a major sequestration form of Ni in Earth near-surface environments.

ACKNOWLEDGMENTS

The nodule samples were kindly provided by D. Baize from INRA, France. The ALS is thanked for the provision of beamtime. A.M. is grateful to LBNL for financial support from the Laboratory Directed Research and Development Program. This work was partly supported by the Director, Office of Energy Research, Office of Basic Energy Sciences, Materials Sciences Division of the U.S. Department of Energy, under contract no. DE-AC03-76SF00098.

REFERENCES CITED

- Baize, D. and Chrétien, J. (1994) Les couvertures pédologiques de la plate-forme sinémurienne en Bourgogne: particularités morphologiques et pédogéochimiques. *Etude et Gestion des Sols*, 2, 7–27.
- Brown, G.E., Foster, A.L., and Ostergren, J.D. (1999) Mineral surfaces and bioavailability of heavy metals: A molecular-scale perspective. *Proceedings of the National Academy of Sciences, U.S.A.*, 96, 3388–3395.
- Buseck, P.R. (1992) Minerals and reactions at the atomic scale: Transmission electron microscopy, vol. 27. *Reviews in Mineralogy*, Mineralogical Society of America, Washington, D.C.
- Childs, C.W. (1975) Composition of iron-manganese concretions from some New Zealand soils. *Geoderma*, 13, 141–152.
- Chukhrov, F.V. and Gorshkov, A.I. (1981) Iron and manganese oxide minerals in soils. *Transactions of the Royal Society, Edinburgh*, 72, 195–200.
- Davies, R.A., Islam, M.S., Chadwick, A.V., and Rush, G.E. (2000) Cation dopant sites in the CaZrO_3 proton conductor: a combined EXAFS and computer simulation study. *Solid State Ionics*, 130, 115–122.
- Glasby, G.P., Rankin, P.C., and Meylan, M.A. (1979) Manganiferous soil concretions from Hawaii. *Pacific Science*, 33, 103–115.
- Gomez-Ariza, J.L., Giraldez, I., Sanchez-Rodas, D., and Morales, E. (2000) Selectivity assessment of a sequential extraction procedure for metal mobility characterization using model phases. *Talanta*, 52, 545–554.
- Han, F.X., Banin, A., and Triplett, G.B. (2001) Redistribution of heavy metals in arid-zone soils under a wetting-drying cycle soil moisture regime. *Soil Science*, 166, 18–28.
- Ho, M.D. and Evans, G.J. (2001) Sequential extraction of metal contaminated soils with radiochemical assessment of readsorption effects. *Environmental Science and Technology*, 34, 1030–1035.
- Kirkpatrick, P. and Baez, A.V. (1948) Formation of optical images by X-rays. *Journal of the Optical Society of America*, 38, 766–772.
- Latrille, C., Elsass, F., van Oort, F., and Denaix, L. (2001) Physical speciation of trace metals in Fe-Mn concretions from a rendzic lithosol developed on Sinemurian limestones (France). *Geoderma*, 100, 127–146.
- MacDowell, A.A., Celestre, R.S., Tamura, N., Spolenak, R., Valek, B.C., Brown, W.L., Brawman, J.C., Padmore, H.A., Batterman, B.W., and Patel, J.R. (2001) Submicron X-ray diffraction. *Nuclear Instrument and Method, A* 468, 936–943.
- Manceau, A. and Calas, G. (1986) Ni-bearing clay minerals. 2. X-ray absorption study of Ni-Mg distribution. *Clay Minerals*, 21, 341–360.
- Manceau, A., Llorca, S., and Calas, G. (1987) Crystal chemistry of cobalt and nickel in lithiophorite and asbolane from New Caledonia. *Geochimica et Cosmochimica Acta*, 51, 105–113.
- Manceau, A., Schlegel, M.L., Musso, M., Sole, V.A., Gauthier, C., Petit, P.E., and Trolard, F. (2000) Crystal chemistry of trace elements in natural and synthetic goethite. *Geochimica et Cosmochimica Acta*, 64, 3643–3661.
- Manceau, A., Marcus, M.A., and Tamura, N. (2002) Quantitative speciation of heavy metals in soils and sediments by synchrotron X-ray techniques. In P. Fenter, M. Rivers, N.C. Sturchio, and S. Sutton, Eds., *Applications of Synchrotron Radiation in Low-Temperature Geochemistry and Environmental Science*, in press. *Reviews in Mineralogy and Geochemistry*, Mineralogical Society of America, Washington DC.
- Nriagu, J.O. (1980) *Nickel in the Environment*. Wiley, New York.
- Ostergren, J.D., Brown, G.E., Parks, G.A., and Tingle, T.N. (1999) Quantitative lead speciation in selected mine tailings from Leadville, CO. *Environmental Science and Technology*, 33, 1627–1636.
- Padmore, H.A., Howells, M.R., Irick, S., Renner, T., Sandler, R., and Koo, Y.M. (1996) Some new schemes for achieving high-accuracy elliptical x-ray mirrors by elastic bending. *Society of Photo-Optical Instrumentation Engineers (SPIE)*, 2856, 145–156.
- Palumbo, B., Bellanca, A., Neri, R., and Roe, M.J. (2001) Trace metal partitioning in Fe-Mn nodules from Sicilian soils, Italy. *Chemical Geology*, 173, 257–269.
- Quevauviller, P., Rauret, G., Muntau, H., Ure, A.M., Rubio, R., Lopez-sanchez, J.F., Fiedler, H.D., and Griepink, B. (1994) Evaluation of a sequential extraction procedure for the determination of extractable trace metal contents in sediments. *Fresenius Journal of Analytical Chemistry*, 349, 808–814.
- Rehr, J.J., Mustre de Leon, J., Zabinsky, S.I., and Albers, R.C. (1991) Theoretical X-ray Absorption Fine Structure Standards. *Journal of the American Chemical Society*, 113, 5135–5145.
- Ressler, T. (1998) WinXAS: a Program for X-ray Absorption Spectroscopy Data Analysis under MS-Windows. *Journal of Synchrotron Radiation*, 5, 118–122.
- Rhoton, F.E., Bigham, J.M., and Schulze, D.G. (1993) Properties of iron-manganese nodules from a sequence of eroded fragipan soils. *Soil Science Society America Journal*, 57, 1386–1392.
- Shannon, R.D. (1976) Revised effective ionic radius and systematic studies of interatomic distances in halides and chalcogenides. *Acta Crystallographica*, B25, 925–946.
- Sutton, S.R. and Rivers, M.L. (1999) Hard X-ray synchrotron microprobe techniques and applications. In D. Schulze, P. Bertsch, and J. Stucki, Eds., *Synchrotron X-ray Methods in Clay Science*, p. 146–163. Clay Mineral Society of America, Aurora, CO.
- Tamura, N., Spolenak, R., Valek, B.C., Manceau, A., Meier Chang, N., Celestre, R.S., MacDowell, A.A., Padmore, H.A., and Patel, J.R. (2002) Submicron X-ray diffraction and its applications to problems in materials and environmental science. *Review of Scientific Instruments*, 73, 1369–1372.
- Taylor, R.M., McKenzie, R.M., and Norrish, K. (1964) The mineralogy and chemistry of manganese in some Australian soils. *Australian Journal of Soil Research*, 2, 235–248.
- Teo, B.K. (1986) EXAFS: basic principles and data analysis. 349 p. Springer-Verlag, Berlin.
- Tokashiki, Y., Dixon, J.B., and Golden, D.C. (1986) Manganese oxide analysis in soils by combined X-ray diffraction and selective dissolution methods. *Soil Science Society America Journal*, 50, 1079–1084.
- Vodyanitskii, Y.N., Lesovaya, S.N., and Sivtsov, A.V. (2001) Iron minerals in soils on red-colored deposits. *Eurasian Soil Science*, 34, 774–782.
- Wheating, L.C. (1936) Shot soils of Western Washington. *Soil Science*, 41, 35–45.
- White, G.N. and Dixon, J.B. (1996) Iron and manganese distribution in nodules from a young Texas vertisol. *Journal of the American Soil Science Society*, 60, 1254–1262.
- Yaman, M. (2000) Nickel speciation in soil and the relationship with its concentration in fruits. *Bulletin of Environmental Contamination and Toxicology*, 65, 545–552.

MANUSCRIPT RECEIVED MARCH 22, 2002

MANUSCRIPT ACCEPTED JUNE 20, 2002

MANUSCRIPT HANDLED BY LEE A. GROAT